This is a repository copy of *The Effect of Dynamical Scattering on Single-plane Phase Retrieval in Electron Ptychography*.

White Rose Research Online URL for this paper:
https://eprints.whiterose.ac.uk/205919/

Version: Published Version

Article:

Clark, Laura orcid.org/0000-0001-9471-2743, Martinez, Gerardo T., O'Leary, Colum M. et al. (5 more authors) (2023) The Effect of Dynamical Scattering on Single-plane Phase Retrieval in Electron Ptychography. Microscopy and Microanalysis. pp. 384-394. ISSN 1431-9276

https://doi.org/10.1093/micmic/ozac022

Reuse
This article is distributed under the terms of the Creative Commons Attribution-NonCommercial (CC BY-NC) licence. This licence allows you to remix, tweak, and build upon this work non-commercially, and any new works must also acknowledge the authors and be non-commercial. You don't have to license any derivative works on the same terms. More information and the full terms of the licence here: https://creativecommons.org/licenses/

Takedown
If you consider content in White Rose Research Online to be in breach of UK law, please notify us by emailing eprints@whiterose.ac.uk including the URL of the record and the reason for the withdrawal request.

eprints@whiterose.ac.uk
https://eprints.whiterose.ac.uk/

The Effect of Dynamical Scattering on Single-plane Phase Retrieval in Electron Ptychography

Laura Clark, Gerardo T Martinez, Colum M O'Leary, Hao Yang, Zhiyuan Ding, Timothy C Petersen, Scott D Findlay, Peter D Nellist

Downloaded from https://academic.oup.com/mam/article/29/1/384/6948181 by guest on 24 November 2023

Microscopy and Microanalysis, 2023, **29**, 384–394
https://doi.org/10.1093/micmic/ozac022
Advance access publication 20 December 2022
Original Article

The Effect of Dynamical Scattering on Single-plane Phase Retrieval in Electron Ptychography

Laura Clark[1,*], Gerardo T. Martinez[2,†], Colum M. O'Leary[2,‡], Hao Yang[2], Zhiyuan Ding[2], Timothy C. Petersen[3,4], Scott D. Findlay[3], and Peter D. Nellist[2]

[1]*School of Chemical and Process Engineering, University of Leeds, Leeds LS2 9JT, UK*
[2]*Department of Materials, University of Oxford, Oxford OX1 3PH, UK*
[3]*School of Physics and Astronomy, Monash University, Clayton, Victoria 3800, Australia*
[4]*Monash Centre for Electron Microscopy, Monash University, Clayton, Victoria 3800, Australia*

***Corresponding author:** Laura Clark, E-mail: l.clark@leeds.ac.uk

†Current address: IMEC, Kapeldreef 75, 3001 Leuven, Belgium

‡Current address: Department of Physics and Astronomy, University of California, Los Angeles, CA 90095, USA

Abstract

Segmented and pixelated detectors on scanning transmission electron microscopes enable the complex specimen transmission function to be reconstructed. Imaging the transmission function is key to interpreting the electric and magnetic properties of the specimen, and as such four-dimensional scanning transmission electron microscopy (4D-STEM) imaging techniques are crucial for our understanding of functional materials. Many of the algorithms used in the reconstruction of the transmission function rely on the multiplicative approximation and the (weak) phase object approximation, which are not valid for many materials, particularly at high resolution. Herein, we study the breakdown of simple phase imaging in thicker samples. We demonstrate the behavior of integrated center of mass imaging, single-side band ptychography, and Wigner distribution deconvolution over a thickness series of simulated GaN 4D-STEM datasets. We further give guidance as to the optimal focal conditions for obtaining a more interpretable dataset using these algorithms.

Key words: 4D-STEM, phase retrieval, ptychography, scanning transmission electron microscopy

Introduction

The increasingly widespread adoption and implementation of segmented and pixelated detectors in the scanning transmission electron microscope (STEM) is leading to broader application of algorithms to reconstruct the complex specimen transmission function. Many of these algorithms depend on the multiplicative object approximation and the (weak) phase object approximation, which neglect probe propagation within the sample and dynamic scattering effects. At high resolution on many specimens, these approximations are not strictly valid, but experimental work has suggested that these algorithms may still be useful beyond the limits of strict validity (Yang et al., 2017). To develop a deeper understanding of the utility and breakdown of these imaging algorithms on increasingly thick samples, herein we study a selection of transmission function reconstruction algorithms, as applicable in the STEM. Specifically, we compare integrated center of mass (CoM) imaging, single-side band (SSB) ptychography, and Wigner distribution deconvolution (WDD).

While STEM imaging with segmented detectors is not new (Dekkers & De Lang, 1974; Rose, 1976), the recent increase in the application of segmented and pixelated detectors to materials science problems motivates this work. In particular, atomic-resolution imaging conditions with their associated higher convergence angle have a shallower depth of focus of the electron beam than the large probes used in much of the earlier Lorentz differential phase contrast imaging. The development of aberration correction has allowed for routine atomic resolution imaging using incoherent methods, and segmented and pixelated detectors in STEM create an opportunity to record coherent images including phase images simultaneously with the incoherent modes. An electron beam used to form atomic resolution images in an aberration corrected instrument (e.g. a 14.4 mrad semi-convergence angle at 300 keV) will have a depth of field of approximately 9.5 nm (Borisevich et al., 2006). This is often of the same scale as the sample thickness, so must be considered for data to be accurately interpreted (Vulović et al., 2014). By way of contrast, the 500 μrad probes used for Lorentz STEM have depths of field of the order of 1 μm, which can then be neglected for typical sample thicknesses. Whether the (weak) phase object approximation is satisfied will depend on sample material and sample orientation (if the sample is crystalline) (De Graef, 2003; Vulović et al., 2014; Aveyard et al., 2017).

An iterative method combined with a multislice approach to calculating dynamical scattering (Godden et al., 2014) has been shown to allow imaging of atomic columns without apparent dynamical effects (Chen et al., 2021). Contrary to this, single-plane focused-probe ptychographic imaging may

Received: May 16, 2022. **Revised:** August 14, 2022. **Accepted:** September 7, 2022
© The Author(s) 2022. Published by Oxford University Press on behalf of the Microscopy Society of America.
This is an Open Access article distributed under the terms of the Creative Commons Attribution-NonCommercial License (https://creativecommons.org/licenses/by-nc/4.0/), which permits non-commercial re-use, distribution, and reproduction in any medium, provided the original work is properly cited. For commercial re-use, please contact journals.permissions@oup.com

Downloaded from https://academic.oup.com/mam/article/29/1/384/6948181 by guest on 24 November 2023

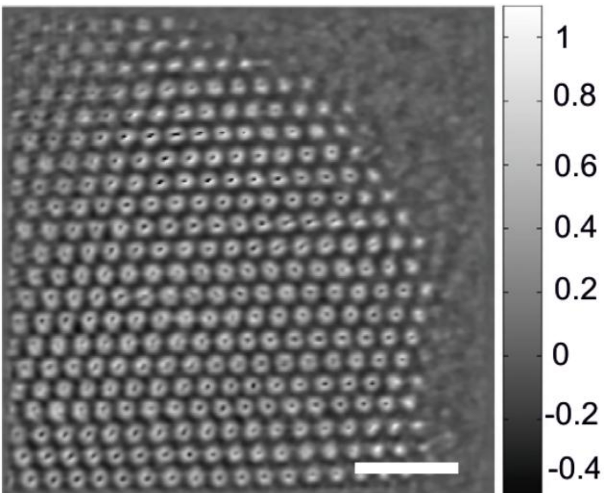

Fig. 1. The reconstructed phase of the complex transmission function of a gold nanoparticle reconstructed using the Wigner distribution deconvolution method with correction of residual aberrations. Note the central-dip in the atomic columns towards the center of the particle is absent from atomic columns at the (thinner) edge regions of the nanoparticle. Scale bar 1 nm, color bar in radians. Figure adapted from Figure 4c of Yang et al. (2017).

only be strictly valid for very thin samples at atomic resolution. Previous work has demonstrated that the images remain high-contrast, and with atomic-column localization for sample thicknesses of practical interest, even in high-Z materials (Yang et al., 2017). An example of this is highlighted in Figure 1, where the atomic contrast is still clear at all column positions, even in this strongly scattering gold nanoparticle. Each column profile however has either a smooth peak profile or a caldera profile. With this experimental data in mind, and with reference to previous studies of the limitations of segmented detector DPC imaging (Close et al., 2015; Müller-Caspary et al., 2017; Winkler et al., 2020), we seek to explore the breakdown of the single-plane transmission function reconstruction algorithms currently available to the STEM community for full four-dimensional scanning transmission electron microscopy (4D-STEM) datasets obtained on pixelated detectors. In this work, our goal is to demonstrate the range of experimentally useful imaging conditions for 4D-STEM at atomic resolution. To investigate this, we simulate 4D-STEM datasets for a thickness series of crystalline GaN specimens. We consider thicknesses between 3 and 175 Å thick (1–55 unit cells), i.e. from a single unit cell to values beyond what is typically used for "thin" sample simulations (Close et al., 2015; Müller-Caspary et al., 2017; Winkler et al., 2020). A comparison of the resultant images from different 4D-STEM analyses allows for clarification of experimentally useful sample conditions for successful imaging.

We begin with a review of detector geometries and the relevant imaging algorithms, before presenting the images obtained in each mode through a thickness series of GaN and discussing the experimentally appropriate ranges of each.

Segmented and Pixelated Detectors

STEM imaging (Fig. 2a) with segmented detectors has been in use since the 1970s (Dekkers & De Lang, 1974; Rose, 1976) with early applications in the study of nanoscale magnetic phenomena (Chapman et al., 1992). Traditional bright field (BF)

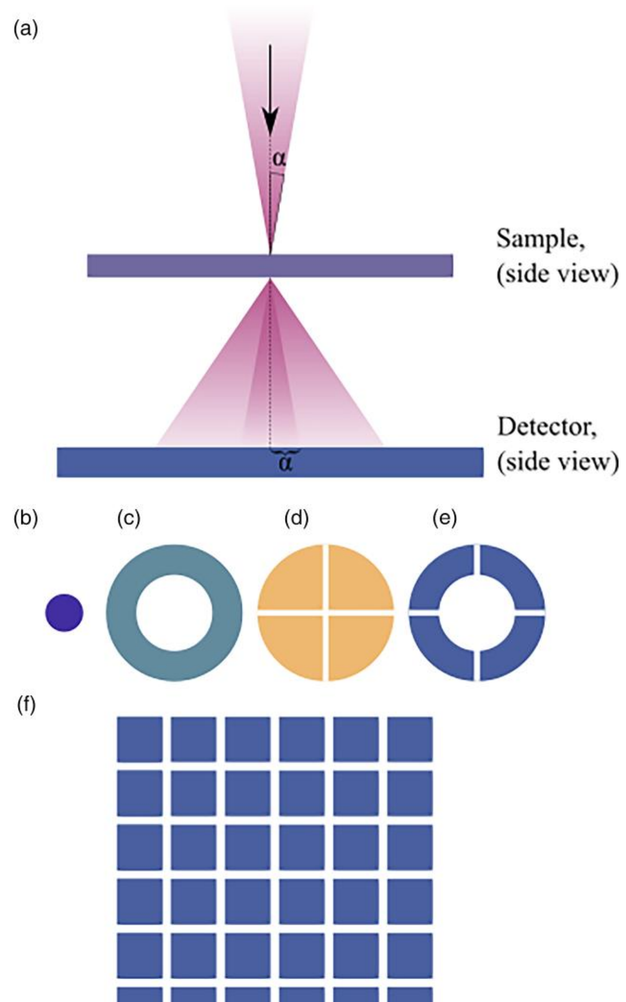

Fig. 2. Schematic illustration 4D-STEM experiments. (**a**) Side view of STEM experiment. The lower panels show popular detector geometries, (**b**) bright field, (**c**) annular dark field, (**d**) quadrant-segmented, (**e**) annular quadrant-segmented, and (**f**) pixelated.

(Fig. 2b) or annular dark field (ADF) (Fig. 2c) detectors allow for a measurement of the proportion of beam intensity remaining on axis or scattered to high angles, respectively. They integrate the scattering intensity azimuthally, within their collection radii. Segmented detectors (Fig. 2d), however, allow for a deeper level of interrogation of the collected scattered electrons, such as a comparison of intensities landing on opposing detector segments. Subsequent developments included the annular segmented detector (Fig. 2e) for improved signal-to-noise measurements (Chapman et al., 1990), and detectors with multiple annuli and segments (Haider et al., 1994; Shibata et al., 2010) for improved sensitivity and precision.

Implementation of pixelated detectors (Fig. 2f) in recent years can be seen as a natural extension of this trend in which detector pixels can be considered as segments of a finely divided detector. The data obtained by these detectors can be partitioned and manipulated as the user wishes—STEM images from "virtual" detectors can be viewed live, or after data collection (Ciston et al., 2019). The remainder of this article deals with pixelated detector datasets, but the same considerations should apply to all 4D-STEM detector systems.

Pixelated detectors introduce some challenges. First, the acquisition time per probe position can be slow, which may lead

Downloaded from https://academic.oup.com/mam/article/29/1/384/6948181 by guest on 24 November 2023

to image distortion due to sample drift (though recent developments in fast pixelated detectors are ameliorating this issue). Second, the size of a STEM dataset scales with the number of detector pixels, and can be in the region of 10 GB for 256^2 scan positions across a 256^2 pixel detector. However, neither challenge is overly restrictive with modern equipment (Nord et al., 2020; Paterson et al., 2020).

Phase Imaging Methodologies

In the STEM, there is considerable flexibility in the shape, size, and arrangement of our electron detectors. By selecting these appropriately, we can control what information about the sample our dataset (and thus resultant image) is sensitive to.

For example, the conventional on-axis BF-STEM detector, as in Figure 2a, allows imaging of elastically scattered electrons with a simple experimental setup (Carter & Williams, 1996). An ADF detector (Fig. 2b) with sufficiently high inner angle will be sensitive to electrons scattered by the nuclear potential and can allow counting of the atomic nuclei across the image (Li et al., 2008; Aveyard et al., 2014).

In the multiplicative approximation, where we model the sample as a single transmission function,

$$\mathrm{T}(\mathbf{x}) = |\mathrm{T}(\mathbf{x})| \exp(\mathrm{i}\phi(\mathbf{x})), \tag{1}$$

variations in $|T(\mathbf{x})|$ are often negligible, and the properties of interest are only detectably encoded in the phase, $\phi(\mathbf{x})$. That variations in $|T(\mathbf{x})|$ are often negligible is why the multiplicative approximation is frequently referred to as the phase object approximation (Vulović et al., 2014). Phase contrast imaging methods allow us to extract this information, through using a range of different detector geometries and data processing algorithms. The methodologies most commonly employed in phase contrast STEM are described in the following subsections.

Differential Phase Contrast and Center of Mass Imaging

The phase of the transmission function can reveal the structure of electromagnetic fields within a sample and how these vary across the field of view. The electromagnetic fields within a sample can be treated by following either a ray optics model or a wave optics model. According to ray optics, the Lorentz force (i.e. $\mathbf{F} = q(\mathbf{E} + \mathbf{v} \times \mathbf{B})$), causes the electron beam to be deflected by an angle proportional to the fields it has traversed. Alternatively, in a wave optics model, the Fourier shift theorem describes how the shift of beam intensity in the detector plane is caused by the phase gradient of the specimen transmission function in the sample plane (Goodman, 2005). If the field-induced phase gradients are constant across the width of the STEM probe, this shift will be uniform, while variations in the specimen on the length-scale of the probe will lead to deformation in the BF disc intensities (Cao et al., 2018; Clark et al., 2018).

Segmented detectors allow these field-induced shifts to be detected through taking the difference in intensity in orthogonal directions as the probe is rastered across the sample (Rose, 1976). Annular quadrant detectors (such as in Fig. 2e) can allow for improved signal-to-noise in cases where the shift is proportionately small compared with the BF disc diameter (Shibata et al., 2010). Increasing measurement precision comes with increasing numbers of segments or direct CoM measurement (Schwarzhuber et al., 2018).

Images formed of the BF disc-shift at each probe position can be scaled to give the phase gradient of the specimen transmission function—these are termed differential phase contrast (DPC) STEM images, and permit atomic resolution imaging of the specimen's electrostatic potential (Müller et al., 2014). Images formed from the increasingly sub-divided detectors allow a more precise measurement of the CoM shift of the BF disc per probe position and are sometimes termed CoM-STEM images.

These images, as pairs of orthogonal phase gradients, can be combined and integrated (De Jonge et al., 2008; Lazić et al., 2016) to give the phase of the specimen transmission function, termed iDPC or iCoM STEM images (this nomenclature choice typically depends on whether segmented or pixelated detectors are used). In this study, we use iCoM images from pixelated detector datasets as these allow a more direct comparison to the other phase imaging methods we consider.

Scanning Transmission Electron Microscopy Ptychography

The 4D datasets resulting from pixelated detectors can, however, be analyzed in a variety of other ways. One such family of methods is focused-probe direct ptychography, which comprises both the SSB and WDD methods (Rodenburg & Bates, 1992; Pennycook et al., 2019). We note that ptychography can be performed with as few as three detector segments (McCallum et al., 1995; Brown et al., 2016), but the resultant image may have residual artifacts (Yang et al., 2015). The probe convergence angle limits the contrast transfer function, and in turn affects the dose-efficiency of the method for imaging a given system (Seki et al., 2018; O'Leary et al., 2020). There also exists a family of iterative (i.e. nondirect) ptychographic algorithms. There are many variations to choose from, and here we select the extended ptychographic iterative engine (ePIE) (Maiden & Rodenburg, 2009; Rodenburg & Maiden, 2019) method to compare against the direct methods as it is one of the more widely applied algorithms (Gao et al., 2017; Song et al., 2018; O'Leary et al., 2020).

Both SSB and WDD analyses begin from 4D datasets of intensities, $|M(\mathbf{K}_f, \mathbf{R}_p)|^2$, collected in the micro-diffraction plane, in which $\mathbf{K}_f$ denotes detector coordinate in reciprocal space, and $\mathbf{R}_p$ denotes probe position in real space. Applying the phase object approximation M can be described as

$$M(\mathbf{K}_f, \mathbf{R}_p) = \int a(\mathbf{R} - \mathbf{R}_p)\psi(\mathbf{R}) \exp(2\pi \mathrm{i}\mathbf{K}_f \cdot \mathbf{R})\, d\mathbf{R}, \tag{2}$$

in which $A(\mathbf{K}_f) = |A(\mathbf{K}_f)| \exp(\mathrm{i}\chi(\mathbf{K}_f))$ describes an aberrated aperture function and typically is a disc of uniform intensity, and $a(\mathbf{R}) = \mathcal{F}(A(\mathbf{K}_f))$, where $\mathcal{F}$ denotes a Fourier transform. $\psi(\mathbf{R})$ is the complex specimen transmission function.

To filter the sample information from the 4D data, we follow Yang et al. (2017) and begin by Fourier transforming the collected intensities, $|M|^2$, with respect to $\mathbf{R}_p$:

$$\begin{aligned} &G(\mathbf{K}_f, \mathbf{Q}_p) \\ &\quad = A(\mathbf{K}_f)A^*(\mathbf{K}_f + \mathbf{Q}_p) \otimes_{\mathbf{K}_f} \Psi(\mathbf{K}_f)\Psi^*(\mathbf{K}_f - \mathbf{Q}_p). \end{aligned} \tag{3}$$

Here, $\mathbf{Q}_p$ is the spatial frequency of probe positions. The superscript asterisk denotes complex conjugation, and Ψ is the Fourier transform of ψ. At this point, the two methods, SSB and WDD ptychography, differ as while both methods rely on the phase object approximation, SSB further requires the *weak* phase object approximation.

Downloaded from https://academic.oup.com/mam/article/29/1/384/6948181 by guest on 24 November 2023

Single-Side Band Ptychography

If we apply the weak phase object approximation to equation (3) and thus disregard any scattering effects beyond first order, G can be simplified, following Pennycook et al. (2015), and expressed as a sum of three terms:

$$\begin{aligned} G(\mathbf{K}_f, \mathbf{Q}_p) = &|A(\mathbf{K}_f)|^2 \delta(\mathbf{Q}_p) \\ &+ A(\mathbf{K}_f)A^*(\mathbf{K}_f + \mathbf{Q}_p)\Psi_s^*(-\mathbf{Q}_p) \\ &+ A^*(\mathbf{K}_f)A(\mathbf{K}_f - \mathbf{Q}_p)\Psi_s(+\mathbf{Q}_p), \end{aligned} \quad (4)$$

where $\Psi_s(\mathbf{Q}_p)$ is the Fourier transform of the scattered object transmission function at spatial frequency $\mathbf{Q}_p$ (Rodenburg et al., 1993). As such, G at a particular $\mathbf{Q}_p$ can be described by three discs of intensity: the unscattered disc and two scattered discs. For $\lambda|\mathbf{Q}_p| < 2\alpha$, these discs will overlap to some extent. The wavefunctions within the disc overlaps will interfere and thus allow us access to phase information of the object transmission function. Integrating the complex value from one of the double overlap regions for each $\mathbf{Q}_p$ will give a complex 2D dataset, $\Psi(\mathbf{Q}_p)$ (Pennycook et al., 2015). Taking our information from only this overlap region effectively constitutes applying a spatial-frequency-dependent noise filter: image information is only selected from spatial frequency regions in the data where the weak-phase approximation implies the information should be. This explains the particularly noise-robust behavior of this algorithm (O'Leary et al., 2020). One further Fourier transform brings us back to $\psi(\mathbf{R}_p)$, our real space object transmission function.

The choice of which set of $\mathbf{Q}_p$ disc overlaps to use (i.e. term 2 or term 3 of equation (4)) leads to only a contrast inversion and can be freely chosen.

Wigner Distribution Deconvolution

The Wigner method proceeds from equation (3) with an inverse Fourier transform with respect to $\mathbf{K}_f$. Here, we follow the notation and derivation of Yang et al. (2017), leading to:

$$\begin{aligned} H(\mathbf{R}, \mathbf{Q}_p) = &\int a^*(\mathbf{b})a(\mathbf{b}+\mathbf{R}) \exp(-2\pi i \mathbf{Q}_p \cdot \mathbf{b})\, d\mathbf{b} \\ &\times \int \psi^*(\mathbf{c})\psi(\mathbf{c}+\mathbf{R}) \exp(-2\pi i \mathbf{Q}_p \cdot \mathbf{c})\, d\mathbf{c} \end{aligned} \quad (5)$$

which is a product of two Wigner distribution functions: one of the probe properties, and one of the sample properties. These can then be separated using a Wigner deconvolution. Following this with a further Fourier transform, one reaches:

$$D(\mathbf{K}_f, \mathbf{Q}_p) = \Psi(\mathbf{K}_f)\Psi^*(\mathbf{K}_f - \mathbf{Q}_p). \quad (6)$$

This 4D function, $D(\mathbf{K}_f, \mathbf{Q}_p)$, can be condensed to 2D by selecting the $\mathbf{K}_f = 0$ plane

$$\Psi(\mathbf{Q}_p) = \frac{D^*(0, \mathbf{Q}_p)}{\sqrt{D(0, 0)}}. \quad (7)$$

A subsequent Fourier transform reconstructs $\psi(\mathbf{R}_p)$, the complex object transmission function in real space.

Extended Ptychographic Iterative Engine

The ePIE algorithm developed by Maiden & Rodenburg (2009), is a modified version of the earlier Ptychographic Iterative Engine (PIE), developed by Rodenburg & Faulkner (2004). PIE proceeds using a similar 4D dataset to that discussed above and an assumed model for the shape of the electron beam at the sample plane. From an initial model of the sample, a guess of the first diffraction pattern is made—and compared with that in the dataset. Corrections to the model of the sample are made iteratively until an overall error metric converges (Rodenburg & Faulkner, 2004). The ePIE algorithm further allows for the assumed model of the shape of the electron beam to be iteratively corrected (Maiden & Rodenburg, 2009; Rodenburg & Maiden, 2019).

Comparisons between the Phase Imaging Modes

The above discussion demonstrates that while WDD and iCoM techniques are mathematically applicable to a broader range of samples than SSB, as they avoid the additional condition imposed by the weak phase object approximation, the SSB has a strong Fourier filter, removing frequencies which cannot be accurately transmitted in this optical setup. From this, it is not immediately obvious which method will behave most predictably in thicker specimens.

In experimental materials science, there are further criteria of concern. Physical electron microscope imaging will also be limited by finite drift (of the sample, or the lens settings). With this, the feasible speed of data acquisition becomes important. Conventional monolithic detectors (e.g. BF, HAADF, or segmented-detector DPC), operating at up to 10 MHz, are much faster than most of the presently available pixelated detectors (Ishikawa et al., 2020). Pixelated datasets as required for the ptychography methods investigated here necessitate higher sampling in the detector plane—pixelated detectors typically operate at frame rates in the range of 1–8 kHz, although state-of-the-art prototype detectors are now approaching frame rates of 87 kHz (Ciston et al., 2019; Pelz et al., 2021). An intermediary option can be provided by a segmented-annular detector array with fourfold symmetry and several annuli (Shibata et al., 2010) or a few pixel array (Yang et al., 2015).

However, many samples are beam-sensitive, in that they are easily damaged by the electron beam in the process of imaging (Egerton, 2019; Ilett et al., 2020; Bustillo et al., 2021). In these situations, we may need to consider which imaging methods allow for higher dose-efficiency of the electron beam. It turns out that this ordering is an almost perfect inversion of the imaging speed ordering listed above, with BF-STEM least efficient, DPC moreso, and the ptychography methods most efficient (Yang et al., 2015; Seki et al., 2018; O'Leary et al., 2020). The dose-efficiency comparison between the direct SSB and WDD methods and iterative methods such as ePIE cannot be trivially made: optimum ePIE collection conditions are expected to differ as it need not have a focused probe and at reduced dose the convergence of the algorithm is less stable (Bunk et al., 2008).

As such, the decision of which imaging mode is most suitable for a given sample on a given microscope is nontrivial. In this paper, we seek to guide the reader as to which methods may give the most interpretable data.

Results and Discussion

Localized Atomic Column Contrast

The behavior of 4D-STEM imaging methods in a thickness series of crystalline samples was investigated by simulating datasets using muSTEM (Allen et al., 2015, 2022), assuming

Downloaded from https://academic.oup.com/mam/article/29/1/384/6948181 by guest on 24 November 2023

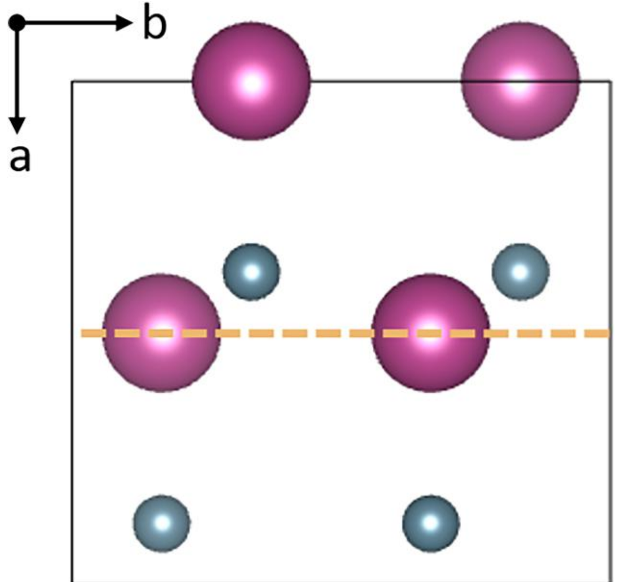

Fig. 3. GaN orthorhombic cell as used for muSTEM, imaged along the [2 $\bar{1}$ $\bar{1}$ 0] axis. The yellow (dashed) line indicates the plane in which the data was taken for Figure 4. Ga atoms are depicted as magenta (large), with N atoms depicted as teal (small). Figure created using Vesta (Momma & Izumi, 2011).

perfect spatial coherence, of a thickness series of GaN (1–55 unit cells) along the [2 $\bar{1}$ $\bar{1}$ 0] axis, with the electron probe (semi-convergence angle $\alpha = 14.4$ mrad, accelerating voltage 300 keV) focused on the top surface of the sample. Further simulation details are compiled in the Appendix. The resultant data are then analyzed according to a range of imaging algorithms (BF, DF, iCoM, SSB, WDD, and ePIE) and compared with BF-TEM simulations. An orthorhombic supercell model of GaN was generated to allow for simple muSTEM input and is illustrated in Figure 3. Thermal effects are accounted for using the quantum excitation of phonons model available within muSTEM (which for the present purposes is computationally equivalent to the frozen phonon model, though with different conceptual underpinnings (Forbes et al., 2010)).

For an initial comparison, WDD ptychographic phase maps through the GaN thickness series are visualized in the x–z plane, slicing through the crystal vertically, and compared with BF-TEM imaging. This is illustrated in Figure 4. For the thin sample case (1–5 unit cells), illustrated in the upper row of Figure 4, all signals remain localized on-column, but with more contrast and improved signal localization in the phase methods than the (directly available) BF-TEM intensity. For thicker samples, the lower row of Figure 4 shows that the WDD contrast remains significantly more localized on-column, at each thickness, than the equivalent BF-TEM intensity, and slightly more localized on-column than the BF-TEM phase. At 35–40 unit cells thick, in the BF-TEM intensity case the contrast has shifted significantly away from the column position while the BF-TEM phase is unclear and could mislead. At these same thicknesses, the WDD contrast remains close to symmetric around the column positions, throughout several contrast inversions (observable in Fig. 4f at slices 15, 40, and 55). This indicates that the WDD images are more directly interpretable than an equivalent BF-TEM intensity image. We also note that the caldera profiles in the WDD series

Downloaded from https://academic.oup.com/mam/article/29/1/384/6948181 by guest on 24 November 2023

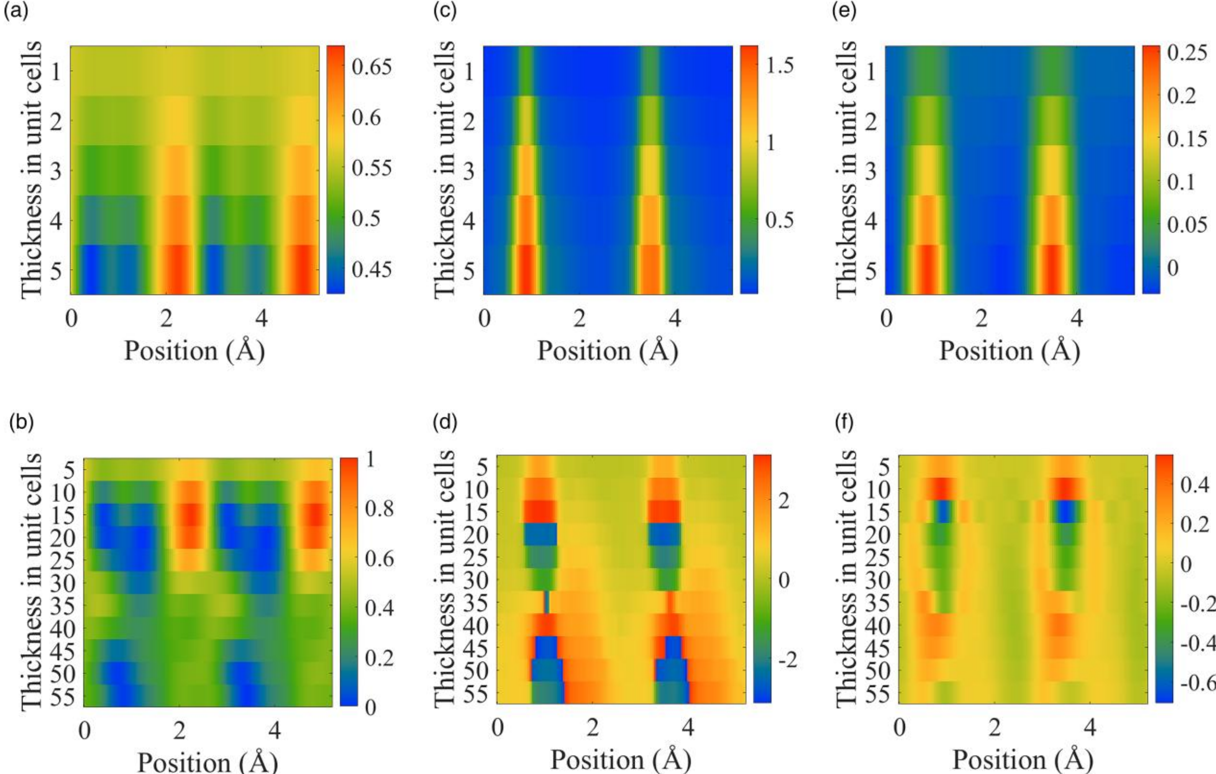

Fig. 4. Image profiles through the x–z plane, along the plane indicated by the dashed line in Figure 3. Upper row: 1–5 unit cells thick, lower row: 5–55 unit cells thick. (**a**,**b**) BF-TEM intensity (color bar in a.u.), (**c**,**d**) BF-TEM phase (color bar in radians), (**e**,**f**) WDD ptychography phase (color bar in radians). Perceptually uniform color map following Kovesi (2015, 2022).

occur at similar thicknesses to the phase wrapping in the BF-TEM phase.

The x–z plots of Figure 4 indicate that ptychographic phase imaging may be well-behaved for even thick samples, well beyond where one might expect the multiplicative object approximation to be valid. We note that at the zero-aberration conditions simulated, the BF-TEM image intensities are likely to show little contrast. Phase contrast can be generated by the use of aberrations to generate a phase plate. The phase of the exit wave in the TEM case is shown in Figure 5. The closely spaced Ga and N columns are only resolved as separate peaks for the thinnest samples ($< \approx 30$ unit cells). The phase profile rapidly becomes difficult to interpret at higher thicknesses, with phase wrapping and phase singularities hindering the unwrapping processes (Allen et al., 2001).

Caldera Profiles at Atomic Positions

To compare different imaging modes further, here we compare the x–y maps of the GaN unit cell through the thickness

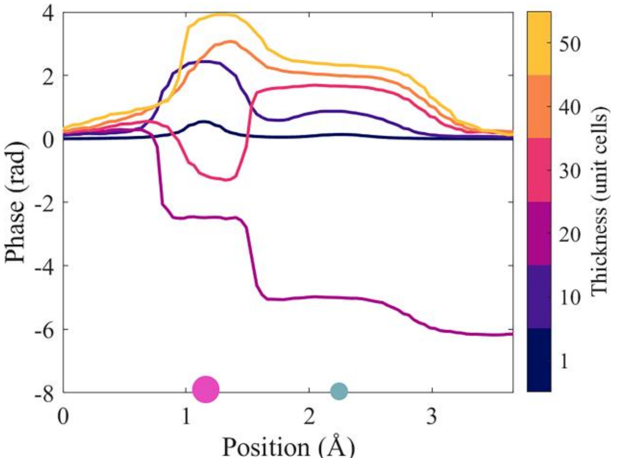

Fig. 5. Line profiles through TEM exit wave phase plots at different thicknesses, in the direction of closest alignment between Ga and N. The positions of the atoms are indicated on the x-axis (Ga: magenta, larger; N: teal, smaller).

series (3.19–175 Å or 1–55 unit cells), for each of the imaging methods of interest here (BF, annular DF, iCoM, SSB, and WDD). The BF detector had an outer collection angle of 0.2α and the DF detector was set to 1.05α–2α, while iCoM, SSB and WDD were processed as presented above. It is assumed that the illuminating probe was focused on the incident surface of the sample.

In Figure 6, we observe that the phase methods (SSB, WDD, and iCoM) are well behaved for the thinnest samples ($\leq$10 unit cells). At 15 cells, the SSB, WDD, and ePIE modes first develop caldera-like contrast, previously mentioned in Figure 1. From 20 to 30 cells thick, the caldera feature is also observable in the iCoM maps. Contrast reversal as seen in the BF-TEM simulations of Figure 4 and phase wrapping as in Figure 5 occur near the onset-thickness of these calderas. However, after this thickness range, conventional atomic column profiles are recovered in the STEM imaging modes. From around 40 cells thick, it becomes increasingly difficult to locate the atomic column positions in the iCOM, SSB, and WDD images, with SSB, WDD, and ePIE also showing some artifact peaks away from the atomic sites. These artifact peaks are not visible in the iCoM images which may be a result of the greater area of integration used in this data (Nellist & Pennycook, 1999).

The robustness of HAADF imaging to dynamic effects has been ascribed to the integration over the detector which leads to an incoherent imaging model (Nellist & Pennycook, 1999). We note that direct ptychographic reconstruction methods, and the iCOM method, have an integration over regions of the detector plane, unlike BF imaging, which may be an explanation of the improved localization seen in direct ptychography and iCOM. The SSB and WDD cases show similar image features due to their similar contrast transfer functions (O'Leary et al., 2020). The ePIE shows broadly the same features (caldera and artifact peaks) as the other ptychographies.

Thickness Effects in Aberration Correction

A further advantage of employing ptychography algorithms is that they can allow for postacquisition aberration correction (Yang et al., 2016), provided sufficient sampling and SNR in the collected dataset. This can be helpful for experimental low-

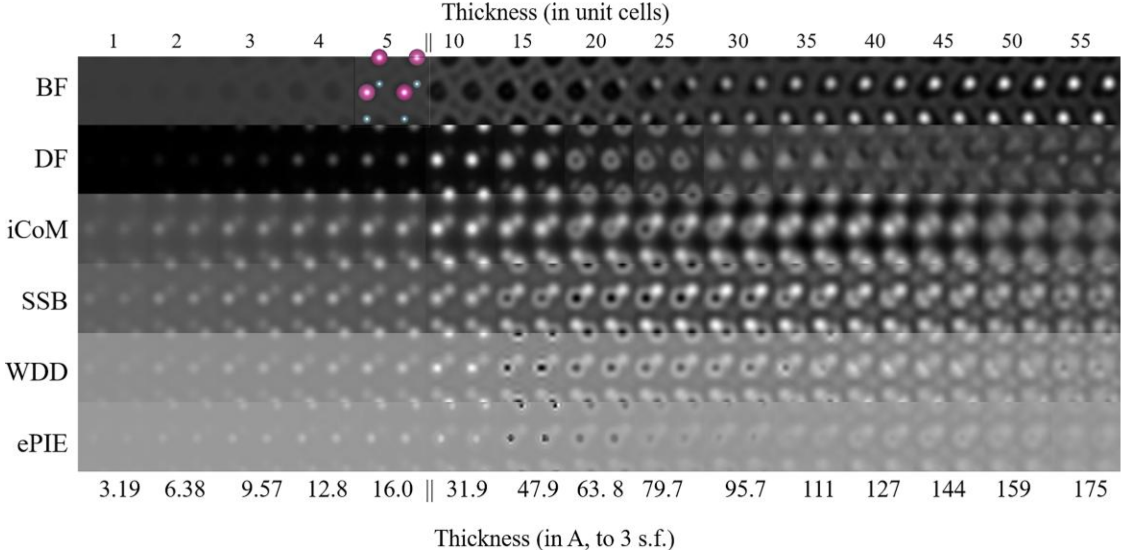

Fig. 6. Image reconstructions in the top-surface focus condition, with sample thicknesses from 1 to 55 unit cells thick, imaged in BF, DF, iCoM, SSB, WDD, and ePIE modes. The overlay indicates atomic positions, Ga atoms: magenta (large) and N atoms: teal (small) (Momma & Izumi, 2011).

Downloaded from https://academic.oup.com/mam/article/29/1/384/6948181 by guest on 24 November 2023

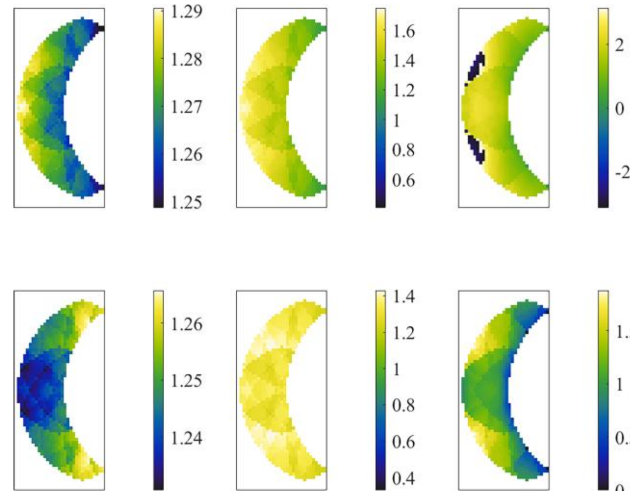

Fig. 7. Illustration of phase interference in double overlap regions for 3, 31, and 175 Å thick samples (left to right) in the top surface focus case (upper panel) and the mid-plane focus condition (lower panel). Perceptually uniform color map following Kovesi (2015, 2022).

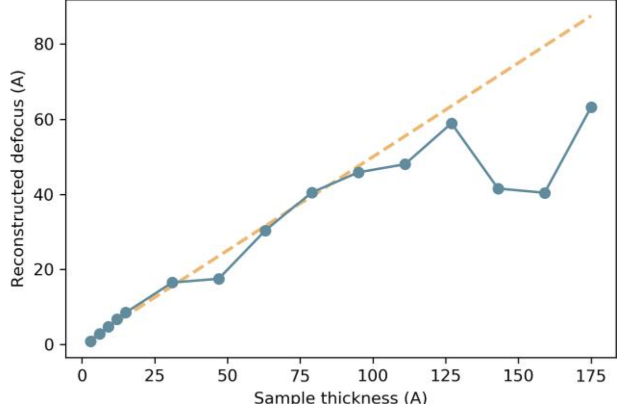

Fig. 8. Reconstructed defocus versus input sample thickness (circle markers and blue (solid) line) in the top-surface focal condition. The yellow (dashed) line indicates an underfocus of 0.5× sample thickness.

dose imaging (Pennycook et al., 2019). For a thin sample and with zero residual aberrations, the phase of the overlap regions given by equation (4) will be uniform, which allows the simple summation approach of the SSB method to be applied. This occurs because the phase of the diffracted beams is not affected by the incident beam direction. Residual aberrations lead to phase variations over the disc overlaps, and it is these variations that are used to detect the residual aberrations. Dynamical diffraction and beam propagation, however, lead to diffracted beam phases which depend on incident beam direction, and therefore the phase in the disc overlap regions will start to vary. This can be seen in Figure 7. At low thickness, the phase variation is small, demonstrated by the narrow range of the color bars. As the thickness increases, a left-to-right phase ramp is seen. Such a phase ramp is similar to the phase ramp caused by defocus aberrations (see Appendix A). Perhaps unsurprisingly, the primary effect of increasing thickness is to introduce an apparent defocus aberration. One can employ a singular value decomposition matrix inversion aberration detection algorithm (described in Supplementary Material of Yang et al., 2016) to reconstruct an effective defocus for each thickness. This is shown in Figure 8. It can be seen that up to about 125 Å, the reconstructed defocus corresponds to half of the sample thickness. Consequently, this suggests that the phase distortion due to specimen thickness could be minimized by a STEM probe focused half way through the sample. This aligns with expectations from previous studies (Plamann & Rodenburg, 1998; Close et al., 2015).

Figure 9 shows the transition from flat phase (3 Å sample: purple lines, theory, and simulation overlap in this case) to defocus-induced linear gradient in phase (31 Å sample, teal lines, theory is shown with the dashed, fine line and simulation with the thick, dashed line; we see good agreement between these two profiles) to complex structure in the phase (175 Å sample simulation, yellow lines; here we see the simulation (thick, dash-dot) line diverging from the trend of the simple theoretical model (fine, dash-dot)). If the phase structure was modulated only by the defocus due to sample thickness, the data extracted from simulations would be expected to coincide well with the theoretical predictions at all thicknesses, while in Figure 9, we see that this holds well for the 3 and 31 Å thick specimens and but not for the 175 Å case: as such, we note that the thickness-induced defocus model breaks down as multiple scattering becomes significant. In Figure 10, with the probe focused at the sample mid-plane, we see that there is less phase variation across the double-overlap region: the variation in phase is negligible for the 3 and 31 Å thick specimens, and the phase across the 175 Å double overlap region is generally flatter than in Figure 9.

The comparison between Figures 9 and 10 therefore suggests a way to improve the imaging conditions: reduce the aberrations in the dataset by collecting data with the probe focused at half the specimen thickness. Towards this, we present images formed with a probe focused at the sample mid-plane in Figure 11 and the associated reconstructed defocus versus thickness plot in Figure 12. With this focus adjustment, the iCoM, SSB, WDD, and ePIE images remain interpretable with the intensity remaining more strongly on-column

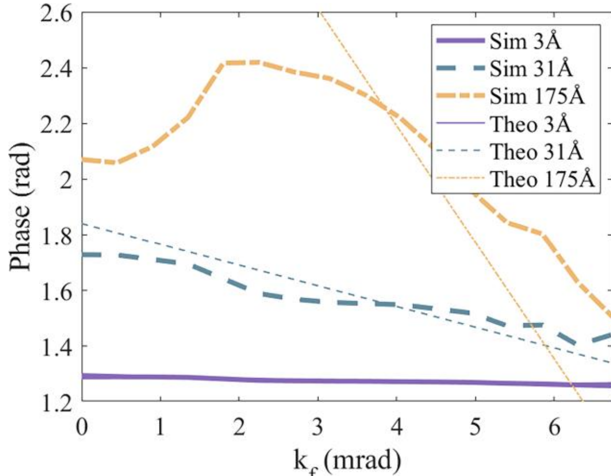

Fig. 9. Line profiles of the phase extracted from the double overlap regions presented in the simulated data of Figure 7, upper-panel, compared with theoretical thickness induced defocus (further discussed in Appendix A). Profile taken horizontally at the widest point of each left-hand overlap region.

Downloaded from https://academic.oup.com/mam/article/29/1/384/6948181 by guest on 24 November 2023

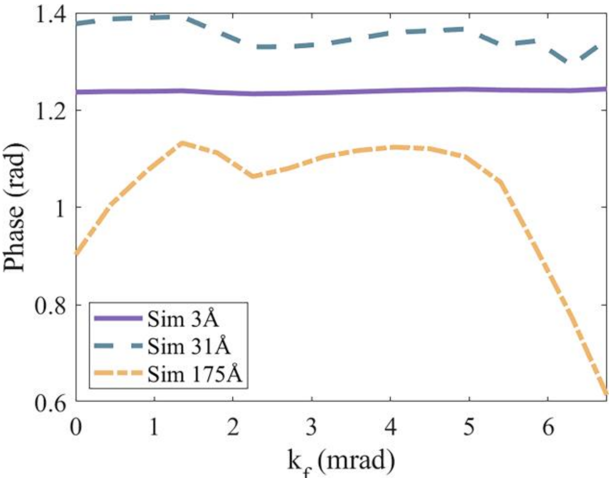

Fig. 10. Line profiles of the phase extracted from the double overlap regions presented in Figure 7, lower-panel. Profile taken horizontally at the widest point of each left-hand overlap region.

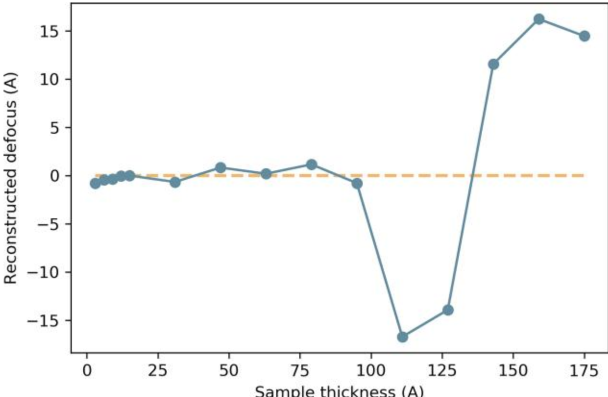

Fig. 12. Reconstructed defocus versus input sample thickness (circle markers and blue (solid) line) in the mid-plane focal condition. The yellow (dashed) line indicates 0 defocus.

throughout this thickness series of 1–55 unit cells thick and the artifacts at the nonatomic sites are now eliminated. iCoM, SSB, and WDD methods are similarly dose efficient (Seki et al., 2018; O'Leary et al., 2020), and the demonstration that these dose efficient methods can also be directly interpretable confirms the importance and applicability of these techniques. The phase across the disc overlaps in Figure 7 under these adjusted focal conditions shows much less variation. The analysis of the effective aberrations across the thickness series in this focal condition is presented in Figure 12. The effective defocus aberration remains close to zero until around 100 Å thick in this scenario.

A natural extension of measuring aberrations in a 4D-STEM dataset is then to seek to correct for these aberrations. This method has previously been demonstrated on a weakly scattering sample (Yang et al., 2016). Here, we choose to apply postacquisition aberration correction to the 111 Å thick samples, as at this thickness the dynamical scattering has a strongly visible impact in the reconstructed phases presented in Figures 6 and 11, the aberrations are significant at this thickness. To judge the impact of postacquisition aberration correction compared with preacquisition focus tuning, we now directly compare the WDD phase maps from (a) a mid-plane focused dataset without postacquisition aberration correction, (b) a top-surface focused dataset without postacquisition aberration correction and (c) a top-surface focused dataset with postacquisition aberration correction, as presented in Figure 13. By inspection of these maps, we find that postacquisition aberration correction improves localization of the top plane focus acquisition dataset, such that features are located on column again—but cannot remove the caldera artifact which occurs at high thicknesses. As such, postacquisition aberration correction improves signal localization and thus identification of atomic columns, but cannot be relied on for quantitative data when significant dynamical scattering has occurred. In such a case, further adjustments may be employed such as multislice ptychography (Chen et al., 2021).

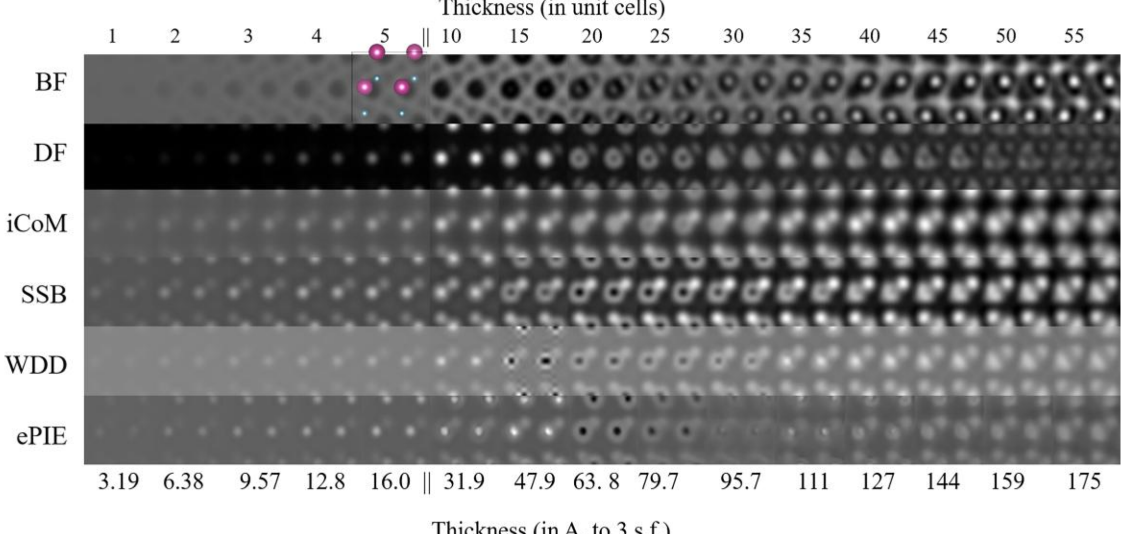

Fig. 11. Image reconstructions in the mid-plane focus condition, with sample thicknesses from 1 to 55 unit cells thick, imaged in BF, DF, iCoM, SSB, WDD, and ePIE modes. The overlay indicates atomic positions, Ga atoms: magenta (large) and N atoms: teal (small) (Momma & Izumi, 2011).

Downloaded from https://academic.oup.com/mam/article/29/1/384/6948181 by guest on 24 November 2023

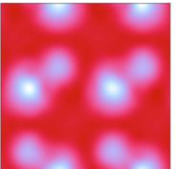
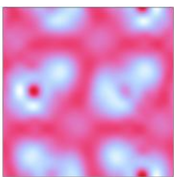
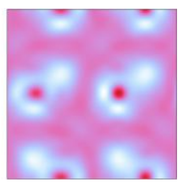

Fig. 13. Phase maps produced by the Wigner distribution deconvolution method on 111 Å thick GaN. Left panel: mid-plane focus probe, no aberration correction applied. Mid-panel: top plane focus probe, no aberration correction applied. Right panel: top plane focus probe, postacquisition aberration correction applied. Perceptually uniform color map following Kovesi (2015, 2022).

Conclusions

A study of 4D-STEM phase imaging methods over a thickness series of GaN samples reveals that the studied 4D-STEM imaging methods (SSB, WDD, iCoM, and ePIE), are rather robust to dynamical scattering effects, with image intensity remaining strongly localized on atomic column positions. It is suggested that this occurs because ptychography and iCOM methods involve a level of integration across the detector plane, which is also the mechanism through which HAADF imaging leads to localization through incoherence (Nellist & Pennycook, 1999). While fully quantitative interpretation of the phase images may not be feasible at higher thicknesses, the work presented here does suggest that atomic column positions remain relatively reliable in direct ptychography and iCoM reconstructions even beyond their conventional thickness limits of applicability.

It is also shown that the initial effect of increasing thickness is to introduce an apparent defocus aberration that has a value of half of the sample thickness. This suggests an approach by which the apparent localization can be further enhanced through optimization of the optical condition upon acquisition. Specifically, we demonstrate that application of these imaging methods is significantly improved with the STEM probe focused in the mid-plane of the specimen, with atomic columns identifiable in iCoM, SSB, WDD, or ePIE imaging of GaN through to 55 unit cells (175 Å) thick. Even when the probe is focused on the entrance surface of the sample, benefits are seen of reconstructing the ptychography image with a reconstruction defocus of half of the sample thickness.

Acknowledgments

The authors acknowledge Richard Aveyard for simulation discussions and Emanuela Liberti for ptychography calculation discussions.

Financial support

This research was partly supported under the Discovery Projects funding scheme of the Australian Research Council (Project No. DP160102338). This project has received funding from the European Union's Horizon 2020 research and innovation programme under the Marie Skłodowska-Curie grant agreement No. 891504. Support is gratefully acknowledged from the EPSRC (EP/K040375/1 "South of England Analytical Electron Microscope"), the Henry Royce Institute for Advanced Materials (EP/R00661X/1, EP/S019367/1, and EP/R010145/1) and grant number EP/M010708/1. Financial support was also received from the EU H2020 Grant No. 823717 ESTEEM3.

Conflict of interest

The authors declare that they have no competing interest.

References

Allen LJ, Brown HG, D'Alfonso AJ, Findlay SD & Forbes BD (2022). muSTEM github repository. Available at: https://github.com/HamishGBrown/MuSTEM

Allen LJ, D'Alfonso AJ & Findlay SD (2015). Modelling the inelastic scattering of fast electrons. *Ultramicroscopy* **151**, 11–22.

Allen LJ, Faulkner HML, Oxley MP & Paganin D (2001). Phase retrieval and aberration correction in the presence of vortices in high-resolution transmission electron microscopy. *Ultramicroscopy* **88**, 85–97.

Aveyard R, Ferrando R, Johnston RL & Yuan J (2014). Modeling nanoscale inhomogeneities for quantitative HAADF STEM imaging. *Phys Rev Lett* **113**, 075501.

Aveyard R, Zhong Z, Batenburg KJ & Rieger B (2017). Optimizing experimental parameters for the projection requirement in HAADF-STEM tomography. *Ultramicroscopy* **177**, 84–90.

Borisevich AY, Lupini AR & Pennycook SJ (2006). Depth sectioning with the aberration-corrected scanning transmission electron microscope. *Proc Natl Acad Sci USA* **103**, 3044–3048.

Brown HG, D'Alfonso AJ, Chen Z, Morgan AJ, Weyland M, Zheng C, Fuhrer MS, Findlay SD & Allen LJ (2016). Structure retrieval with fast electrons using segmented detectors. *Phys Rev B* **93**, 134116.

Bunk O, Dierolf M, Kynde S, Johnson I, Marti O & Pfeiffer F (2008). Influence of the overlap parameter on the convergence of the ptychographical iterative engine. *Ultramicroscopy* **108**, 481–487.

Bustillo KC, Zeltmann SE, Chen M, Donohue J, Ciston J, Ophus C & Minor AM (2021). 4D-STEM of beam-sensitive materials. *Acc Chem Res* **54**, 2543–2551.

Cao MC, Han Y, Chen Z, Jiang Y, Nguyen KX, Turgut E, Fuchs GD & Muller DA (2018). Theory and practice of electron diffraction from single atoms and extended objects using an EMPAD. *Microscopy* **67**, i150–i161.

Carter CB & Williams DB (1996). *Transmission Electron Microscopy: A Textbook for Materials Science*. New York: Springer Science & Business Media.

Chapman JN, McFadyen IR & McVitie S (1990). Modified differential phase contrast lorentz microscopy for improved imaging of magnetic structures. *IEEE Trans Magn* **26**, 1506–1511.

Chapman JN, Ploessl R & Donnet DM (1992). Differential phase contrast microscopy of magnetic materials. *Ultramicroscopy* **47**, 331–338.

Chen Z, Jiang Y, Shao Y-T, Holtz ME, Odstrčil M, Guizar-Sicairos M, Hanke I, Ganschow S, Schlom DG & Muller DA (2021). Electron ptychography achieves atomic-resolution limits set by lattice vibrations. *Science* **372**, 826–831.

Ciston J, Johnson IJ, Draney BR, Ercius P, Fong E, Goldschmidt A, Joseph JM, Lee JR, Mueller A, Ophus C, Selvarajan A, Skinner DE, Stezelberger T, Tindall CS, Minor AM & Denes P (2019). The 4D camera: Very high speed electron counting for 4D-STEM. *Microsc Microanal* **25**, 1930–1931.

Clark L, Béché A, Guzzinati G, Lubk A, Mazilu M, Van Boxem R & Verbeeck J (2013). Exploiting lens aberrations to create electron-vortex beams. *Phys Rev Lett* **111**, 064801.

Clark L, Brown HG, Paganin DM, Morgan MJ, Matsumoto T, Shibata N, Petersen TC & Findlay SD (2018). Probing the limits of the rigid-intensity-shift model in differential-phase-contrast scanning transmission electron microscopy. *Phys Rev A* **97**, 043843.

Close R, Chen Z, Shibata N & Findlay SD (2015). Towards quantitative, atomic-resolution reconstruction of the electrostatic potential via differential phase contrast using electrons. *Ultramicroscopy* **159**, 124–137.

De Graef M (2003). *Introduction to Conventional Transmission Electron Microscopy*. Cambridge: Cambridge University Press.

De Jonge MD, Hornberger B, Holzner C, Legnini D, Paterson D, McNulty I, Jacobsen C & Vogt S (2008). Quantitative phase imaging with a scanning transmission X-ray microscope. *Phys Rev Lett* **100**, 163902.

Downloaded from https://academic.oup.com/mam/article/29/1/384/6948181 by guest on 24 November 2023

Dekkers NH & De Lang H (1974). Differential phase contrast in a STEM. *Optik* **41**, 452–456.

Dwyer C (2010). Simulation of scanning transmission electron microscope images on desktop computers. *Ultramicroscopy* **110**, 195–198.

Egerton RF (2019). Radiation damage to organic and inorganic specimens in the TEM. *Micron* **119**, 72–87.

Forbes BD, Martin AV, Findlay SD, D'Alfonso AJ & Allen LJ (2010). Quantum mechanical model for phonon excitation in electron diffraction and imaging using a Born-Oppenheimer approximation. *Phys Rev B* **82**, 104103.

Gao S, Wang P, Zhang F, Martinez GT, Nellist PD, Pan X & Kirkland AI (2017). Electron ptychographic microscopy for three-dimensional imaging. *Nat Commun* **8**, 1–8.

PtychoSTEM (2022). Gitlab - ptychostem repository. Available at: https://gitlab.com/alimostaed/ptychoSTEM

Godden TM, Suman R, Humphry MJ, Rodenburg JM & Maiden AM (2014). Ptychographic microscope for three-dimensional imaging. *Opt Exp* **22**, 12513–12523.

Goodman JW (2005). *Introduction to Fourier optics*. Greenwood Village: Roberts and Company Publishers.

Haider M, Epstein A, Jarron P & Boulin C (1994). A versatile, software configurable multichannel STEM detector for angle-resolved imaging. *Ultramicroscopy* **54**, 41–59.

Ilett M, S'ari M, Freeman H, Aslam Z, Koniuch N, Afzali M, Cattle J, Hooley R, Roncal-Herrero T, Collins SM, Hondow N, Brown A & Brydson R (2020). Analysis of complex, beam-sensitive materials by transmission electron microscopy and associated techniques. *Phil Trans R Soc A* **378**, 20190601.

Ishikawa R, Jimbo Y, Terao M, Nishikawa M, Ueno Y, Morishita S, Mukai M, Shibata N & Ikuhara Y (2020). High spatiotemporal-resolution imaging in the scanning transmission electron microscope. *Microscopy* **69**, 240–247.

Kovesi P (2015). Good colour maps: How to design them. arXiv, preprint arXiv:150903700.

Kovesi P (2022). MATLAB and Octave functions for computer vision and image processing. Available at: https://www.peterkovesi.com/matlabfns/

Lazić I, Bosch EGT & Lazar S (2016). Phase contrast STEM for thin samples: Integrated differential phase contrast. *Ultramicroscopy* **160**, 265–280.

Li ZY, Young NP, Di Vece M, Palomba S, Palmer RE, Bleloch AL, Curley BC, Johnston RL, Jiang J & Yuan J (2008). Three-dimensional atomic-scale structure of size-selected gold nanoclusters. *Nature* **451**, 46–48.

Maiden AM & Rodenburg JM (2009). An improved ptychographical phase retrieval algorithm for diffractive imaging. *Ultramicroscopy* **109**, 1256–1262.

McCallum BC, Landauer MN & Rodenburg JM (1995). Complex image reconstruction of weak specimens from a three-sector detector in the STEM. *Optik (Stuttgart)* **101**, 53–62.

Momma K & Izumi F (2011). Vesta 3 for three-dimensional visualization of crystal, volumetric and morphology data. *J Appl Crystallogr* **44**, 1272–1276.

Müller-Caspary K, Krause F, Grieb T, Löffler S, Schowalter M, Béché A, Galioit V, Marquardt D, Zweck J, Schattschneider P, Verbeeck J & Rosenauer A (2017). Measurement of atomic electric fields and charge densities from average momentum transfers using scanning transmission electron microscopy. *Ultramicroscopy* **178**, 62–80.

Müller K, Krause F, Béché A, Schowalter M, Galioit V, Löffler S, Verbeeck J, Zweck J, Schattschneider P & Rosenauer A (2014). Atomic electric fields revealed by a quantum mechanical approach to electron picodiffraction. *Nat Commun* **5**, 1–8.

Nellist PD & Pennycook SJ (1999). Incoherent imaging using dynamically scattered coherent electrons. *Ultramicroscopy* **78**, 111–124.

Nord M, Webster RWH, Paton KA, McVitie S, McGrouther D, MacLaren I & Paterson GW (2020). Fast pixelated detectors in scanning transmission electron microscopy. Part I: Data acquisition, live processing, and storage. *Microsc Microanal* **26**, 653–666.

O'Leary CM, Martinez GT, Liberti E, Humphry MJ, Kirkland AI & Nellist PD (2020). Contrast transfer and noise considerations in focused-probe electron ptychography. *Ultramicroscopy* **221**, 113189.

Paszkowicz W, Podsiadło S & Minikayev R (2004). Rietveld-refinement study of aluminium and gallium nitrides. *J Alloys Compd* **382**, 100–106.

Paterson GW, Webster RWH, Ross A, Paton KA, Macgregor TA, McGrouther D, MacLaren I & Nord M (2020). Fast pixelated detectors in scanning transmission electron microscopy. Part II: Post-acquisition data processing, visualization, and structural characterization. *Microsc Microanal* **26**, 944–963.

Pelz PM, Johnson I, Ophus C, Ercius P & Scott MC (2021). Real-time interactive 4D-STEM phase-contrast imaging from electron event representation data: Less computation with the right representation. *IEEE Signal Process Mag* **39**, 25–31.

Pennycook TJ, Lupini AR, Yang H, Murfitt MF, Jones L & Nellist PD (2015). Efficient phase contrast imaging in STEM using a pixelated detector. Part I: Experimental demonstration at atomic resolution. *Ultramicroscopy* **151**, 160–167.

Pennycook TJ, Martinez GT, Nellist PD & Meyer JC (2019). High dose efficiency atomic resolution imaging via electron ptychography. *Ultramicroscopy* **196**, 131–135.

Plamann T & Rodenburg JM (1998). Electron ptychography. II. theory of three-dimensional propagation effects. *Acta Crystallogr A: Found Adv* **54**, 61–73.

Rodenburg JM & Bates RHT (1992). The theory of super-resolution electron microscopy via wigner-distribution deconvolution. *Phil Trans R Soc Lond A* **339**, 521–553.

Rodenburg JM & Faulkner HML (2004). A phase retrieval algorithm for shifting illumination. *Appl Phys Lett* **85**, 4795–4797.

Rodenburg JM & Maiden A (2019). Ptychography. *Springer Handbook of Microscopy*, pp. 819–904. Switzerland, AG: Springer Nature.

Rodenburg JM, McCallum BC & Nellist PD (1993). Experimental tests on double-resolution coherent imaging via STEM. *Ultramicroscopy* **48**, 304–314.

Rose H (1976). Nonstandard imaging methods in electron microscopy. *Ultramicroscopy* **2**, 251–267.

Schwarzhuber F, Melzl P, Pöllath S & Zweck J (2018). Introducing a non-pixelated and fast centre of mass detector for differential phase contrast microscopy. *Ultramicroscopy* **192**, 21–28.

Seki T, Ikuhara Y & Shibata N (2018). Theoretical framework of statistical noise in scanning transmission electron microscopy. *Ultramicroscopy* **193**, 118–125.

Shibata N, Kohno Y, Findlay SD, Sawada H, Kondo Y & Ikuhara Y (2010). New area detector for atomic-resolution scanning transmission electron microscopy. *J Electron Microsc* **59**, 473–479.

Song B, Ding Z, Allen CS, Sawada H, Zhang F, Pan X, Warner J, Kirkland AI & Wang P (2018). Hollow electron ptychographic diffractive imaging. *Phys Rev Lett* **121**, 146101.

Vulović M, Voortman LM, van Vliet LJ & Rieger B (2014). When to use the projection assumption and the weak-phase object approximation in phase contrast cryo-EM, *Ultramicroscopy* **136**, 61–66.

Winkler F, Barthel J, Dunin-Borkowski RE & Mueller-Caspary K (2020). Direct measurement of electrostatic potentials at the atomic scale: A conceptual comparison between electron holography and scanning transmission electron microscopy. *Ultramicroscopy* **210**, 112926.

Yang H, MacLaren I, Jones L, Martinez GT, Simson M, Huth M, Ryll H, Soltau H, Sagawa R, Kondo Y, Ophus C, Ercius P, Jin L, Kovács A & Nellist PD (2017). Electron ptychographic phase imaging of light elements in crystalline materials using Wigner distribution deconvolution. *Ultramicroscopy* **180**, 173–179.

Yang H, Pennycook TJ & Nellist PD (2015). Efficient phase contrast imaging in STEM using a pixelated detector. Part II: Optimisation of imaging conditions. *Ultramicroscopy* **151**, 232–239.

Yang H, Rutte RN, Jones L, Simson M, Sagawa R, Ryll H, Huth M, Pennycook TJ, Green MLH, Soltau H, Kondo Y, Davis BG & Nellist PD (2016). Simultaneous atomic-resolution electron ptychography and Z-contrast imaging of light and heavy elements in complex nanostructures. *Nat Commun* **7**, 1–8.

Downloaded from https://academic.oup.com/mam/article/29/1/384/6948181 by guest on 24 November 2023

Appendix A

Aberrations in the Overlap Region

The phase structure in the double overlap region, as required for direct electron ptychography, contains features due to the phase of the sample transmission function and features due to the phase of the probe aberration function.

Within an aperture of radius α, the phase surface of the electron beam can be described by an aberration function χ (Clark et al., 2013):

$$\chi = \frac{2\pi}{\lambda}[A_0\theta\cos(\phi-\phi_{11}) + \frac{1}{2}\theta^2\{A_1\cos[2(\phi-\phi_{22})] + C_1\}\ldots], \quad \text{(A.1)}$$

where the phase shifts are described according to their radial angular coordinate $\theta < \alpha$ and azimuthal angular coordinate ϕ. A_0 describes image shift, A_1 twofold astigmatism. The ϕ_{ii} terms describe the relative orientation of the noncircularly symmetric aberrations. In an otherwise corrected microscope, the defocus induced phase shift is thus:

$$\chi = \frac{2\pi}{\lambda}\frac{1}{2}\theta^2 C_1 = \frac{\pi C_1\theta^2}{\lambda}. \quad \text{(A.2)}$$

The overlap region of interest is characterized by one centered aperture function, and one aperture function shifted by an angle of λQ_p, where $\alpha < (\lambda Q_p) < 2\alpha$. Accordingly, the phase in the overlap region due to defocus is:

$$\chi_{\text{overlap}} = \frac{\pi C_1\theta^2}{\lambda} - \frac{\pi C_1(\theta-\lambda Q_p)^2}{\lambda} = \frac{\pi C_1}{\lambda}(2\theta\lambda Q_p - (\lambda Q_p)^2). \quad \text{(A.3)}$$

Thus for an overlap region for a selected λQ_p, the phase will have a linear gradient proportional to the probe defocus.

Appendix B

Simulation and Analysis Parameters

To aid the interested reader, we gather here the relevant parameters used in generating the data presented in this manuscript.

Simulations

- The datasets were simulated using muSTEM (Allen et al., 2015, 2022).
- Probe semi-convergence angle $\alpha = 14.4$ mrad, 300 keV.
- The GaN unit cell potential was divided into two thickness slices per unit cell for propagation, and tiled 8×8 into a supercell.

Fig. B.1. An example of one diffraction pattern, from one probe position, as used in the subsequent analyses.

- Probe step sizes are automatically calculated within muSTEM, and the subsequent images were upsampled using Fourier methods. This Fourier upsampling is exact, as (perfect, simulated) STEM images are bandwidth limited (Dwyer, 2010).
- Convergence was found at 10 phase gratings and 160 Monte Carlo variations (per muSTEM definitions).
- Thermal vibration amplitudes were determined from Paszkowicz et al. (2004).
- The saved 4D-STEM data had the BF disc filling approximately half the width of each 128×128 pixel diffraction pattern—this is the data as-used in the analysis procedures, an example of which is illustrated in Figure B.1.

Analyses

- The analyses were primarily performed using the ptychoSTEM software (PtychoSTEM, 2022).
- The iCoM maps were produced using a python script based on the equations in (De Jonge et al., 2008).
- The BF detector had an outer collection angle of 0.2α.
- The DF detector was set to 1.05α–2α.
- The ePIE analyses presented in this manuscript were produced using codes based on the publications above, developed by Si Gao and Peng Wang (Gao et al., 2017; Song et al., 2018).

Downloaded from https://academic.oup.com/mam/article/29/1/384/6948181 by guest on 24 November 2023